https://doi.org/10.1016/j.ijmecsci.2020.106226

Model-driven Fatigue Crack Characterization and Growth Prediction: A Two-step, 3-D Fatigue Damage Modeling Framework for Structural Health Monitoring

Lei Xu[a], Kai Wang[b], Xiongbin Yang[a], Yiyin Su[a], Jianwei Yang[a], Yaozhong Liao[a], Pengyu Zhou[a], Zhongqing Su [a*]

[a] Department of Mechanical Engineering, The Hong Kong Polytechnic University, Kowloon, Hong Kong SAR

[b] Interdisciplinary Division of Aeronautical and Aviation Engineering, The Hong Kong Polytechnic University, Kowloon, Hong Kong SAR

submitted to ***International Journal of Mechanical Sciences***

(submitted on 15th September 2020; revised and re-submitted on 26th November 2020)

* To whom correspondence should be addressed. Tel.: +852-2766-7818, Fax: +852-2365-4703; Email: Zhongqing.Su@polyu.edu.hk (Prof. Zhongqing Su, *Ph.D*)

Abstract

Prevailing fatigue damage evaluation approaches that make use of the acoustic nonlinearity of guided ultrasonic waves (GUWs) are sustained by simplified models, most of which depict three-dimensional (3-D) fatigue damage in a two-dimensional (2-D) domain [1]. Such approximation risks the evaluation accuracy. With such motivation, this study aspires to a new, two-step modeling framework, aimed at accurately characterizing and continuously monitoring fatigue damage, from its embryonic initiation, through progressive growth to formation of macroscopic crack. In the first step, a 3-D, analytical model based on the theory of elastodynamics sheds light on the generation of contact acoustic nonlinearity in GUWs under the modulation of 'breathing' behavior of a non-penetrating fatigue crack, on which basis a crack-area-dependent nonlinear damage index is yielded. In the second step, a 3-D fatigue crack growth model predicts the continuous growth of the identified fatigue crack in the length and depth along crack front. The framework is validated using numerical simulation, followed with experiment, in both of which the initiation and progressive growth of a real corner fatigue crack is monitored, with continuous prediction of the crack growth in length and depth. Results have demonstrated the accuracy and precision of the developed modeling framework for characterizing embryonic fatigue damage.

***Keywords*:** fatigue crack; non-penetrating crack; structural health monitoring; contact acoustic nonlinearity; crack growth

1. Introduction

Fatigue damage in critical structural components (*e.g.*, fastener holes, bolted joints) is liable for numerous catastrophic accidents of land infrastructure, transportation vehicles, and offshore construction. Early awareness of fatigue damage, in particular the embryonic fatigue cracks, and monitoring of the progressive growth on a regular or even continuous basis are significant yet challenging. Intensive effort over the years has led to diverse evaluation techniques readily available, residing on various mechanisms and principles, which broadly embrace those using acoustic emission [2-4], guided ultrasonic waves (GUWs) [5-8], radiography [9-11], thermographic inspection [12-14], electromagnetic technique [15-17] and eddy current [18-20] to name a few. Amongst them, the GUW-based approaches outperform many others, in virtue of the superb merits that the approaches can offer, including long-range gauging capacity, high sensitivity to damage in small scale, and cost-effectiveness in implementation. The principle of GUW-based evaluation lies in the premise that the propagation attributes of a probing GUW, upon interaction with fatigue damage, are modulated and altered to some extent, and the interaction triggers specific and unique wave scattering phenomena such as wave reflection, transmission, mode conversion, wave energy shift and higher-order harmonics generation; inversely, fatigue damage can be evaluated, via appropriate models and algorithms, by scrutinizing these changes in wave attributes.

Both linear and nonlinear attributes of GUWs have been exploited extensively to accommodate the need of damage characterization. The linear features that are frequently used include the delay in time-of-flight (ToF) [21, 22], degree of energy dissipation [23, 24], mode conversion [25-27], reflection and transmission coefficients of damage-scattered wavefields [28-30]. The use of linear attributes shows particular effectiveness when the characteristic dimensions of damage to be detected are comparable to the wavelength of a probing GUW – a scale at which the damage might have already evolved to a macroscopic degree and sufficed to incur fatal structural failure. However, as envisaged, majority of the fatigue life of a crack remains within a timeframe, during which the crack progresses at a microscopic scale, prior to the formation of macroscopic damage. Both numerical and experimental studies [31, 32] reveal that the duration for a fatigue crack to evolve from its initiation through growth to the formation of a visible crack takes ~80% - 90% of its entire fatigue life. Owing to this, the detectability of the evaluation approaches using linear attributes of GUWs, towards embryonic fatigue damage, is often challenged.

In contrast to linear features, the nonlinear properties of GUWs exhibit higher sensitivity to microscopic damage, and the detectability is not restricted by the wavelength of the probing GUW [33-36]. This makes the excitation of a probing GUW at a high frequency is not of necessity. Approaches in this category are typified by those exploiting higher-order harmonics [37-39], sub-harmonics [40-42], mixed frequency responses [34, 43] and shift in resonance frequency [44]. Representatively, Ramahi *et al.* [45] developed a complementary split-ring resonator (CSRR) to assess sub-millimetre fatigue damage, based on the premise that damage, if any, perturbs the electromagnetic field around CSRR, and consequently results in the shift in resonance frequency. Sohn *et al.* [46] proposed a nonlinear ultrasonic modulation method by calibrating the sideband components captured in spectra under a mixed input of low-frequency and high-frequency GUWs, whereby to evaluate the length of a through-thickness fatigue crack. Qu *et al.* [47] explored nonlinear Rayleigh surface waves, for characterizing stress corrosion cracking (SCC) damage in carbon steel, and discovered phenomenal increase in the measured contact acoustic nonlinearity (CAN) during the early stage of SCC. Jacobs *et al.* [48] proposed a nonlinear ultrasonic technique based on the second harmonic generation (SHG) of surface waves, with which microstructural change and occurrence of microcracks in heterogeneous cement-based materials can be detected. Shen and Giurgiutiu [49] studied the generation of higher-order harmonics of Lamb waves using finite element simulation and established a baseline-free damage index to assess the presence and the severity of cracks. Lee *et al.* [50] utilized the SHG approach to identify fatigue cracks in steel joint and the digital image correlation (DIC) technique was implemented to demonstrate the effectiveness of the method for identification of fatigue crack initiation and growth in joint type structures. Guan *et al.* [51] elaborated the fundamental difference in fatigue crack detection using nonlinear guided waves between plate and pipe structures and found that unlike the plate scenario using nonlinear guided waves, the second harmonic wave generated by the 'breathing' behavior of crack in a pipe had multiple wave modes. A proper damage index which considered all generated wave modes was proposed to quantify the acoustic nonlinearity, facilitating the identification of microscale damage and assessment of the severity of the damage in pipe structures. Earlier, the authors of this study also proposed an analytical model [1, 52], based on the modal decomposition and a variational principle, and proved its effectiveness in capturing CAN generated by a 'breathing' crack and depicting the fatigue crack-disturbed wavefields in both 2-D and 3-D waveguides. A nonlinear damage index derived from that analytical model linked the magnitude of generated second order harmonics to that of the fundamental GUWs, which was validated by evaluating a through-thickness fatigue crack in an aluminium waveguide [1, 53]. Nevertheless, the model, by simplifying a real fatigue crack as a 2-D, through-thickness crack in the waveguide, may present inferior accuracy when the fatigue crack is in its early stage with a non-penetrating pattern.

In majority of the existing work making use of the nonlinearity of GUWs for evaluating small-scale cracks, the crack is approximated to be through the thickness of the waveguide – sort of simplification of a real fatigue crack from its three-dimensional (3-D) reality to two-dimensional (2-D) hypothesis, regardless of the fact that a fatigue crack in its embryonic stage is of a non-penetrating manner, as typified by the semi-elliptical surface cracks and quarter-elliptical corner cracks, in **Fig. 1**. As the non-penetrating stage constitutes the majority of the crack fatigue life [32, 54], such simplification makes evaluation results debatable. Addressing the significance of characterizing and monitoring 3-D, non-penetrating fatigue cracks, Masserey and Fromme [55-57] used an energy-ratio-based method in conjunction with high-frequency ultrasonic waves, to detect a quarter-elliptical corner crack emanating from a fastener hole with an area less than 0.8 mm^2 (equivalent to a cracking area with ~1 mm in length and in depth, respectively), and monitor its growth. A drop in the energy of the ultrasonic pulse amid the crack growth was observed.

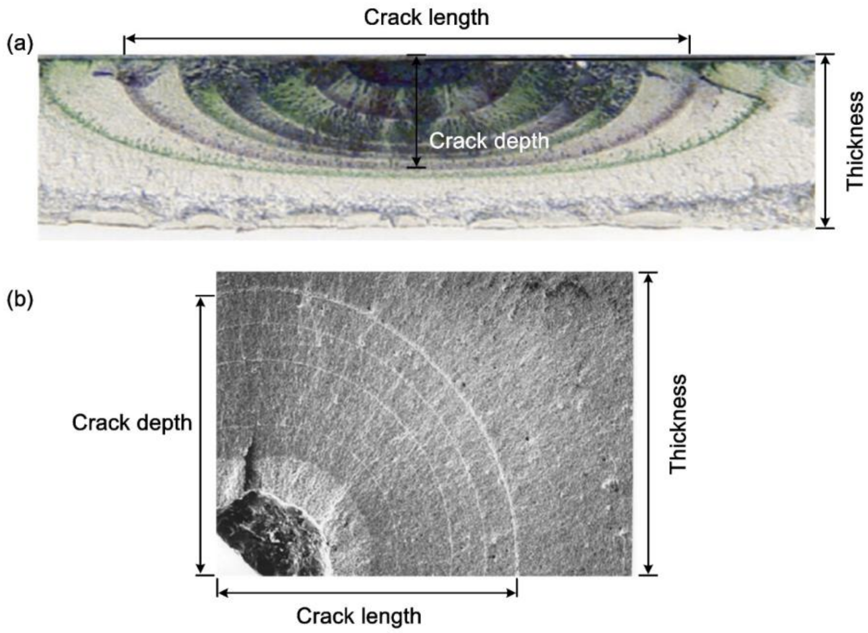

Figure 1. Typical 3-D, non-penetrating fatigue cracks: (a) a semi-elliptical surface crack [58]; and (b) a quarter-elliptical corner crack.

Motivated by this, a two-step fatigue damage modeling framework is developed in this study, aimed at quantitative characterization of both the length and depth of a non-penetrating fatigue crack through its fatigue life. In the first step, a 3-D, analytical model based on the theory of elastodynamics is proposed, for analytically elucidating the generation of CAN in the probing GUW under the modulation of 'breathing' behavior of a non-penetrating fatigue crack. The model yields a crack-area-dependent nonlinear damage index, with which the non-penetrating crack surface area is estimated. In the second step, a 3-D fatigue crack growth model, originated from the fatigue crack growth theory, predicts the shape evolution of the identified crack along its length and depth. A proof-of-concept experiment is performed, in which a real, non-penetrating corner crack, initiated from a fastener hole is continuously monitored, with quantitative prediction of crack progress in both length and depth. Predicted results using the modeling framework are compared against those obtained from numerical simulation and experiment. The key originality of this study lies in substantial and significant extension of an analytical model, for interpreting the interaction between GUWs and 'breathing' crack proposed by the authors in earlier studies [1, 52] which simplify the fatigue crack in a 2-D domain. It aspires to break through the 2-D limitation of the modeling and expand the theoretical framework to a 3-D regime, whereby to accurately and quantitatively describe a real fatigue crack through its entire fatigue life.

2. Two-step Modeling Framework

The proposed modeling framework features an *online phase* and an *offline phase*. In a nutshell, a nonlinear damage index is to be developed in the online phase, by capturing and quantifying SHG, upon the interaction of a probing GUW with the non-penetrating crack, on which basis the surface area of the non-penetrating crack can be estimated; in the offline phase, further evolution of the estimated crack surface is to be predicted via a 3-D fatigue crack growth model, and outputs of the offline phase are the continuous depiction of the crack shape, and a quantitative correlation between the length and depth of the crack during its growth. **Figure 2** recaps this proposed two-step framework.

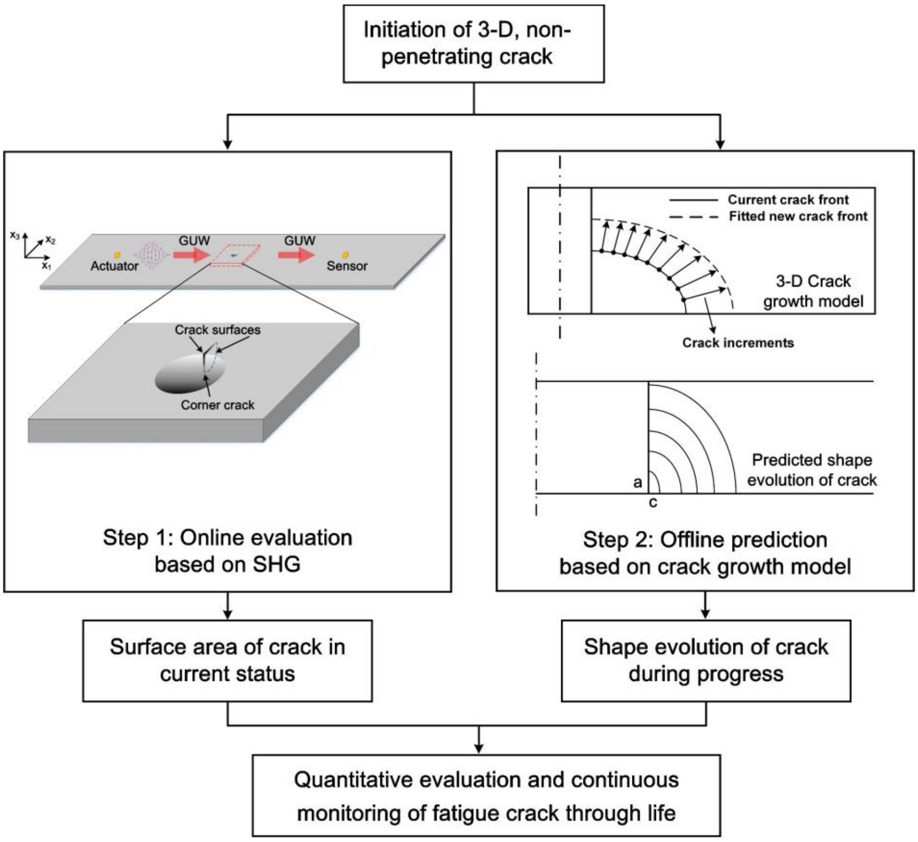

Figure 2. Flowchart of the proposed two-step modeling framework (left column showing the online phase to estimate crack surface area using nonlinear ultrasonic testing; right column showing the offline phase to predict the change in aspect ratio and shape evolution of the crack.

2.1 Online Phase: Evaluation of Non-penetrating Crack Surface

2.1.1 Non-penetrating Crack-induced CAN: *A 3-D Perspective*

CAN is generated under the modulation of a fatigue crack with nonlinear 'breathing' behavior, when a probing GUW traverses the crack. The 'breathing' behavior consists of two alternate periods: 1) during the tensile phase of the probing GUW, two surfaces of the non-penetrating crack are apart from each other, partially or entirely along the waveguide thickness, and this triggers wave scattering and mode conversion at the two surfaces; and 2) during the compressional phase of the probing GUW, two crack surfaces are fully in contact, and this remains GUW propagation undistorted and identical to wave propagation in an intact counterpart waveguide (*i.e.*, an identical waveguide in which the crack does not exist). It is the two alternate periods in a wave cycle, as schematically illustrated in **Fig. 3**, that drive the crack to manifest a 'breathing' behavior. It is noteworthy that in this study, the personified '*breathing*' is used to describe the opening and closing of a fatigue crack that is modulated by the probing GUW when it traverses the crack. Due to the fact that the dimensions of the 3-D, non-penetrating fatigue cracks are minute, it is hypothesized that the entire crack surfaces present the 'breathing' behavior.

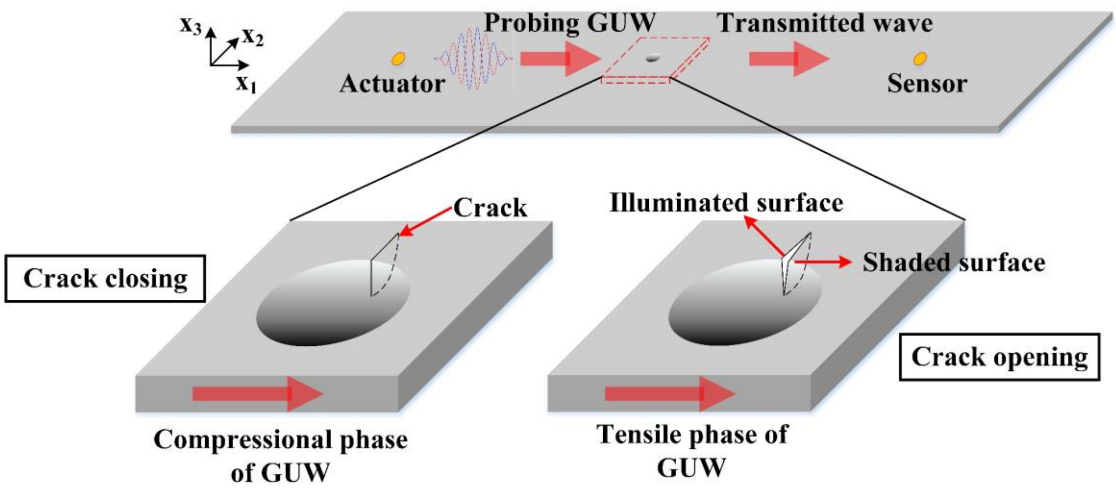

Figure 3. Schematic of two alternate periods of the probing GUW upon interaction with a non-penetrating crack with 'breathing' behavior: crack closing during compressional phase of GUW and crack opening during tensile phase of GUW.

To depict such alternate wave propagation characteristics during the interaction with a fatigue crack, an additional wave source is hypothesized to exist at the crack location, introducing extra wavefield to the original probing GUW. This additional wave source is referred to as '*crack-induced second source*' (CISS) in the authors' previous work [1] (for a 2-D crack scenario). CISS manifests time-dependent traits of the wavefield: it is present when the crack opens, or absent otherwise. CISS is a consequence of the two alternate periods of the 'breathing' behavior of the fatigue crack.

Consider a 'breathing' crack in a stress-free state (*i.e.*, no existing stress around the crack). When the two crack surfaces are apart one from the other, partially or entirely, the open surfaces are traction-free, and the CISS can be defined as a pair of equivalent concentrated forces, each of which is applied on a crack surface. This hypothesis is made based on the fact that the dimensions of the considered non-penetrating fatigue crack are minute. The magnitude of the equivalent force on each crack surface, when crack opens, can be obtained by integrating the stress on the opening area of crack surface as,

$$\left|F_{eq}\right| = \int_{Opening\ area} -\sigma \cdot \overrightarrow{x_1} ds\ , \tag{1}$$

where σ signifies the stress tensor, and $\overrightarrow{x_1}$ the unit direction vector, see **Fig. 3**. The stress at the crack surface is generated by the probing GUW. To include both the open and closed statuses of the crack, CISS can be defined, for a complete wave cycle, using an indicator function, as

$$F_{eq} = \left|F_{eq}\right| \cdot e^{i\omega t} \cdot f(t), \tag{2}$$

where the indicator function $f(t)$ reads

$$f(t) = \begin{cases} 1, & t_{open} < t < t_{close} \\ 0, & t_{close} < t < t_{open} + T. \end{cases} \tag{3}$$

In the above, F_{eq} is the regulated form of CISS, reflecting the 'breathing' behavior of the crack, and ω the angular frequency of the probing GUW. t_{open} and t_{close} are the time when the crack opens and closes, respectively, and T the duration of a wave cycle.

In the model, the time, at which the crack commences to open in a 'breathing' cycle, is deemed as the moment when the probing GUW turns from its compressional phase to a tensile phase; analogously, the time, at which the crack starts to close, is the moment when the probing GUW changes from its tensile phase back to the compressional phase. Considering that the fatigue crack is of 3-D pattern, the displacement of every point on the crack surface, in general, differs from those of other points at a specific moment. Due to the minute dimensions of the non-penetrating fatigue crack, the moment, at which the middle point of the crack surface starts to open (or close), is adopted as the moment for the entire crack to open (or close). With Eq. (2), the higher-order wave modes of the regulated form of CISS resulted from the modulation of the 'breathing' crack can be determined in spectrum via fast Fourier transform. Amongst all the higher-order modes, the second order harmonics at the double excitation frequency (2ω) of the probing GUW can be extracted analytically from the spectrum, as

$$F_{eq}^{2\omega} = A_{2\omega} \cdot \left|F_{eq}\right| \cdot e^{i2\omega t}, \tag{4}$$

where $A_{2\omega}$ denotes the magnitude of the wave mode at the double frequency of excitation.

Recalling elastodynamic analysis [59] and applying it on Eq (4), the full wavefield of the probing GUW in the waveguide can be obtained explicitly, and thus the magnitude of the in-plane displacement in x_1 direction of the CISS-disturbed wavefield at 2ω, denoted by ${}_{2\omega}u_{x_1}$, can be obtained as

$$ {}_{2\omega}u_{x_1} = \sum_{m=0}^{\infty} F_{eq}^{2\omega} \cdot \frac{k_m^{2\omega}}{4i} \cdot \frac{[V_S^m(x_3)]^2}{I_{mm}^S} \cdot [H_0^2(k_m^{2\omega} r) - \frac{1}{k_m^{2\omega} r} H_1^2(k_m^{2\omega} r)]. \quad (5) $$

In the above, $V_S^m(x_3)$ signifies the in-plane displacement of the m^{th}-order symmetric Lamb mode in x_1 direction which varies along the waveguide thickness (x_3), $k_m^{2\omega}$ the wavenumber of the propagating wave at 2ω for the m^{th}-order symmetric Lamb mode, and r the distance between the crack and the location from which the wavefield is captured (*i.e.*, sensor location). i is the imaginary unit and I_{mm}^S the wave energy carried by the m^{th}-order symmetric Lamb mode. $H_p^2(\cdot)$ represents the p^{th}-order Hankel function (p = 0 or 1) of the second kind. For low-frequency GUW, only fundamental Lamb wave mode will be generated in the waveguide, and thus the magnitude of the in-plane displacement in x_1 direction of the CISS-disturbed wavefield at 2ω can be simplified as

$$ {}_{2\omega}u_{x_1}^0 = F_{eq}^{2\omega} \cdot \frac{k_0^{2\omega}}{4i} \cdot \frac{[V_S^0(x_3)]^2}{I_{00}^S} \cdot [H_0^2(k_0^{2\omega} r) - \frac{1}{k_0^{2\omega} r} H_1^2(k_0^{2\omega} r)]. \quad (6) $$

With the obtained amplitude of the CISS-induced symmetric Lamb mode at 2ω, a nonlinear damage index, NI, is defined as

$$ NI = \frac{{}_{2\omega}u_{x_1}^0}{u_{x_1}^{\omega}} = \left|F_{eq}\right| \cdot \frac{A_{2\omega}}{u_{x_1}^{\omega}} \cdot \frac{k_0^{2\omega}}{4i} \cdot \frac{[V_S^0(x_3)]^2}{I_{00}^S} \cdot [H_0^2(k_0^{2\omega} r) - \frac{1}{k_0^{2\omega} r} H_1^2(k_0^{2\omega} r)], \quad (7) $$

where ${}_{2\omega}u_{x_1}^0$ and $u_{x_1}^{\omega}$ represent the magnitudes of the CISS-induced in-plane displacement at double (2ω) and fundamental (ω) excitation frequency, respectively. For an embryonic fatigue crack with tiny dimensions, the probing GUW-induced stress tensor can be regarded constant on each crack surface, and thus the magnitude of CISS ($\left|F_{eq}\right|$) when the crack opens, obtained with Eq. (1), is proportional to the crack surface area. With the nonlinear damage index, a proportional relationship between *NI* and the crack surface area is established, via which the severity of fatigue crack can be calibrated with an experimentally measured *NI*, to be demonstrated in Section 3.

2.1.2 Validation Using Finite Element (FE) Simulation

The relationship between the surface area of a non-penetrating fatigue crack and *NI*, as defined by Eq. (7), is verified using commercial software ABAQUS®/EXPLICIT (experimental validation in Section 3). A plate-like aluminium waveguide (500 mm long, 80 mm wide and 5 mm thick) with a centralized fastener hole (5 mm in radius) is considered, and the developed FE model of the waveguide is shown in **Fig. 4**. A series of through-thickness cracks (2-D scenario) and a series of non-penetrating corner cracks (3-D scenario) of different degrees of severity are respectively simulated. In each simulated case, the crack exists at the fastener hole edge with its cracking surface normal to x_1. For each non-penetrating corner crack, the shape evolution is not considered, as a result of which the crack remains its original quarter-circular patten with the same length (x_2) and depth (x_3), as shown in **Fig.4**. Material properties of the waveguide are listed in **Tab. 1**. Three third order elastic constants (A , B and C) are used in a user-defined subroutine (VUMAT) to introduce the intrinsic material nonlinearity into the model, along with the nonlinearity generated by the 'breathing' behavior of the crack.

Table 1. Material properties of the aluminum waveguide in FE simulation.

Density (kg/m^3)	Elastic modulus (GPa)	Poisson's ratio	A (GPa)	B (GPa)	C (GPa)
2700	73	0.33	-320	-200	-190

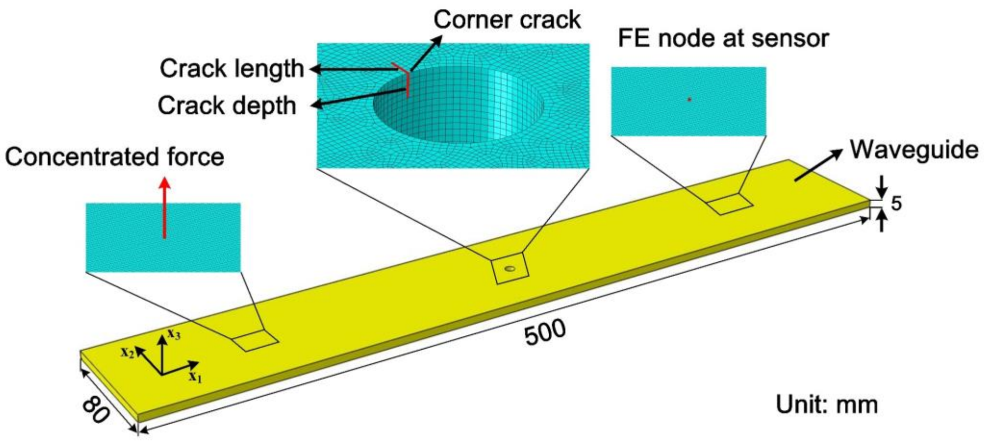

Figure 4. FE model of the considered waveguide bearing a non-penetrating crack.

An Hanning window-modulated 5-cycle sinusoidal toneburst is excited at a central frequency of 180 kHz, by applying a pair of point-type forces on the upper and lower surfaces of the waveguide, **Fig. 4**. The elements of the waveguide boundary are defined in virtue of *absorbing layer by increasing damping* (ALID), which dissipates wave energy reflected from the boundary. To model the 'breathing' behavior of the fatigue crack, a surface-surface contact pair definition is applied, with which the two crack surfaces can only be either in contact or apart from each other. To strengthen the second order harmonics induced by the crack, which usually have weak magnitudes compared with those of the fundamental wave modes, a pulse-inversion approach [60] is used. In the approach, two identical probing GUWs, with the same magnitude but in opposite phase, are excited, respectively, for each simulated case. The second order harmonics induced by the 'breathing' crack, under two excitation conditions with opposite phase, are respectively captured, summation of which leads to a magnitude twice the original magnitude of the respectively generated second order harmonics, as well as cancellation of the fundamental wave mode.

With the pulse-inversion approach, the ‘breathing’ crack-induced second order harmonics are intensified, which is conducive to feature extraction. **Figure 5(a)** illustrates a typical probing GUW signal and the second order harmonics generated by the modeled crack. The short-time Fourier transform (STFT) converts the captured GUW signals from the time domain to the time-frequency domain to ascertain the wave components at ω and 2ω. **Figure 5(b)** displays the spectrum of the probing GUW, and **Figs. 5(c-e)** the spectra of the second order harmonics obtained from an intact waveguide and other two scenarios: one containing a through-thickness crack and the other containing a non-penetrating crack, in both of which the crack length is the same.

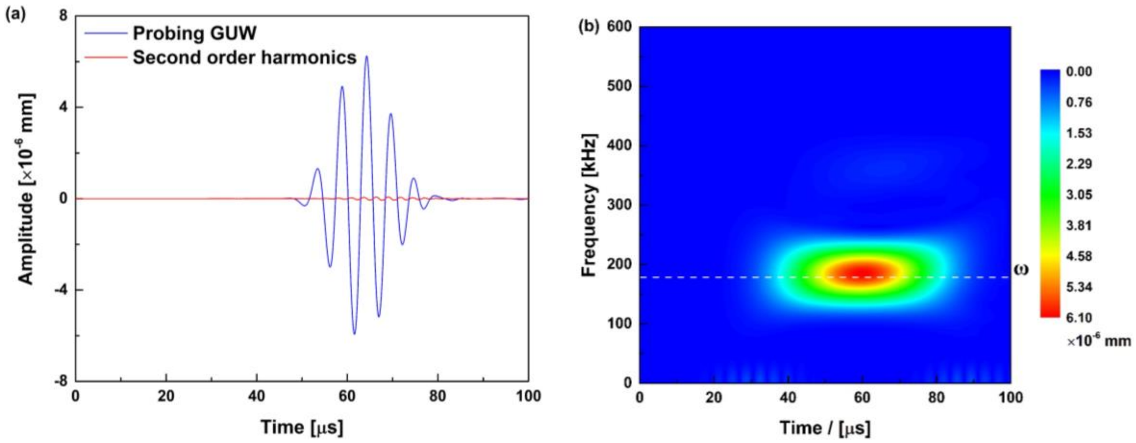

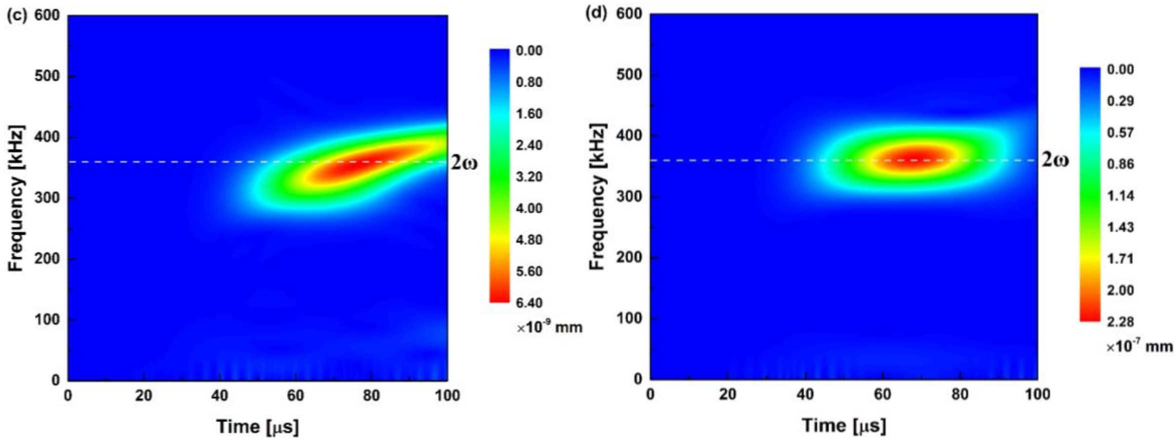

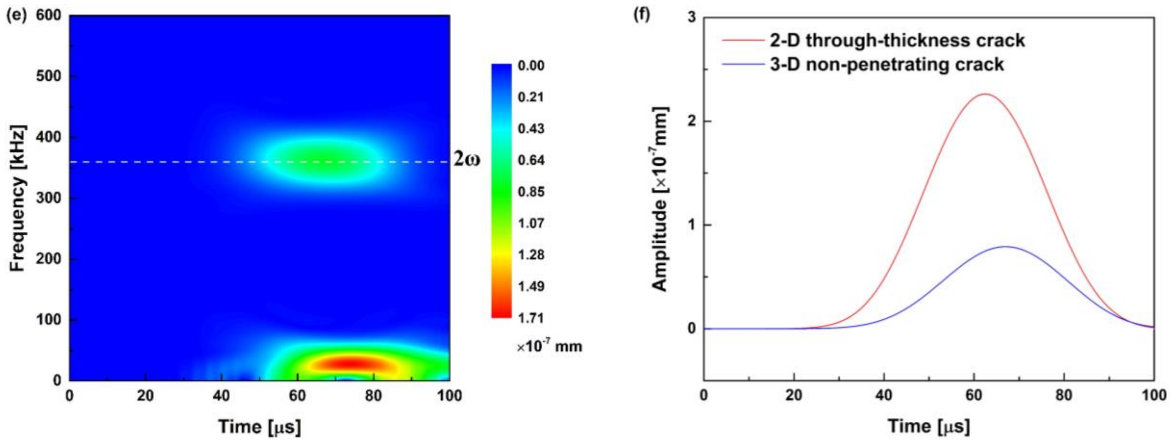

Figure 5. (a) A probing GUW signal captured from the waveguide bearing a 'breathing' crack and the crack-induced second order harmonics; (b) spectrum of the probing GUW in (a); spectra (showing the second order harmonics) for (c) an intact waveguide, (d) the waveguide containing a through-thickness crack, and (e) the waveguide containing a non-penetrating crack; (f) comparison of the amplitudes of the second order harmonics generated by the penetrating and non-penetrating cracks.

Compared with the intact status, the magnitude of the second order harmonics captured from the waveguide with a crack, either through-thickness or non-penetrating, is intensified, which is ascribed to the modulation of the 'breathing' behavior of the crack on the probing GUW. It is also noteworthy that the magnitude of the second order harmonics induced by the through-thickness crack is stronger than that induced by the non-penetrating crack, as seen in **Figs. 5(f)** – a consequence of the larger crack surface of the through-thickness crack compared with the non-penetrating crack when the lengths of the two cracks are the same (the former is of a rectangular shape, while the latter is quarter-circular), which accounts for a stronger CISS.

With ascertained magnitudes of the crack-induced second order harmonics, the nonlinear damage index is calculated according to Eq. (7). **Figure 6** shows the calculated index against variation in crack length and crack surface area, for both the through-thickness and non-penetrating cracks.

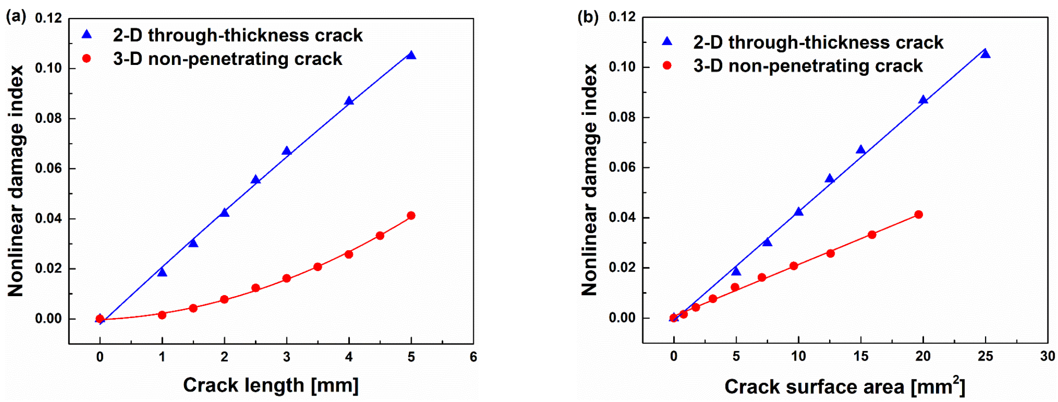

Figure 6. Nonlinear damage index versus (a) crack length, and (b) surface area of through-thickness and non-penetrating cracks (the damage index of the through-thickness crack increases linearly against crack length, while that of the non-penetrating crack increases in parabolic advance; when plotted with respect to crack surface area, the indices of both the through-thickness and non-penetrating cracks vary linearly).

As observed in **Fig. 6(a)**, *NI* increases proportionally with the crack length for a penetrating crack, while it increases in parabolic advance for a non-penetrating crack. This can be attributed to the fact that the surface area of a penetrating crack increases linearly as the crack progresses; it is therefore that the magnitude of CISS and *NI*, both of which are proportional to the crack surface area, consequently increase linearly with respect to the crack length. In contrast, a non-penetrating crack progresses in both the length and depth directions simultaneously, leading to a parabolic relationship between the crack length (or depth) and the surface area, and showing an increase of *NI* against the crack length (or depth) in parabolic advance. On the other hand, when plotted with regard to the crack surface area, **Fig. 6(b)**, *NI*, for both the penetrating and non-penetrating cracks, varies proportionally to the surface area, and this observation tallies with the conclusion drawn in above theoretical analysis (Section 2.1.1) that the nonlinear damage index is proportional to the crack surface area. FE simulation results demonstrate the feasibility of using the proposed nonlinear damage index for evaluating the area of a fatigue crack quantitatively, for both penetrating and non-penetrating scenarios.

2.2 Offline Phase: Crack Growth Prediction

The 3-D, non-penetrating crack investigated in the above FE simulation is quarter-circular in shape, and its length is identical to the depth initially. It is important to articulate that the growth rates of a non-penetrating fatigue crack along its length and depth are different in general, due to the different stress states at the crack front. In reality, a corner crack is usually quarter-elliptical and its aspect ratio (*i.e.*, the ratio of crack depth to length) is variable during crack progress [61]. To continuously evaluate of the length and depth of the fatigue crack that has already been identified using the above online phase, the shape evolution of the crack is further predicted using the second step of the proposed modeling framework – the *offline phase*. In this phase, no probing GUW is generated to interact with the crack. The core of the *offline phase* is a crack growth model, with which a relationship between the respective increase in the crack length and in the crack depth can be achieved, according to the updated crack size obtained from the *online phase*. This enables continuous depiction of the crack growth. It is such continuous update and monitoring of the crack growth that makes this two-step framework outperforms conventional approaches which only predict the fatigue crack growth based on the initial crack size.

2.2.1 Shape Evolution of a Non-penetrating Crack

The growth of a 2-D, through-thickness crack through its fatigue life can be determined in terms of the Paris's law and the classical Paris-Erdogan equation, as

$$\frac{dl}{dN} = C(\Delta K)^n, \qquad (8)$$

where l is the crack severity (length or depth) and N is the cycle number of the fatigue load. $\frac{dl}{dN}$ signifies the crack growth increment in a single fatigue load cycle, and ΔK the *stress intensity factor* (SIF) *range* at the crack tip which is known to be the main driving force leading to continuous crack growth. C and n are the Paris's law parameters related to fatigue properties of the material. An accurate SIF at the crack front guarantees faithful characterization of crack evaluation.

A predictive model, taking the effect of crack closure phenomenon into consideration, is developed in the offline phase, to estimate the respective progress in length and depth of a 3-D, non-penetrating fatigue crack. The model resides on a twofold hypothesis:

1) the shape of the non-penetrating fatigue crack remains a semi-ellipse for a surface crack, and a quarter-ellipse for a corner crack; and
2) the growth direction of all points on the crack front in a fatigue cycle is perpendicular to the crack front, from which the crack initiates.

Taking a quarter-elliptical corner crack at a fastener hole as an example, **Fig. 7**, the SIF (K) of each point on the crack front can be calculated in terms of the Newman-Raju empirical equation as follows [62]

$$K = S\sqrt{\pi \frac{a}{Q}} F(\frac{a}{c}, \frac{a}{t}, \frac{r}{t}, \frac{r}{b}, \frac{c}{b}, \phi), \quad (9)$$

where S is the external applied stress; ϕ is the parametric angle of the quarter-elliptical crack front; a and c are the depth and length of the crack, respectively; t denotes the thickness of the waveguide; $2b$ and $2H$ are the width and height of the waveguide, respectively; r is the radius of the fastener hole, and Q an empirical shape factor for a quarter-elliptical corner crack.

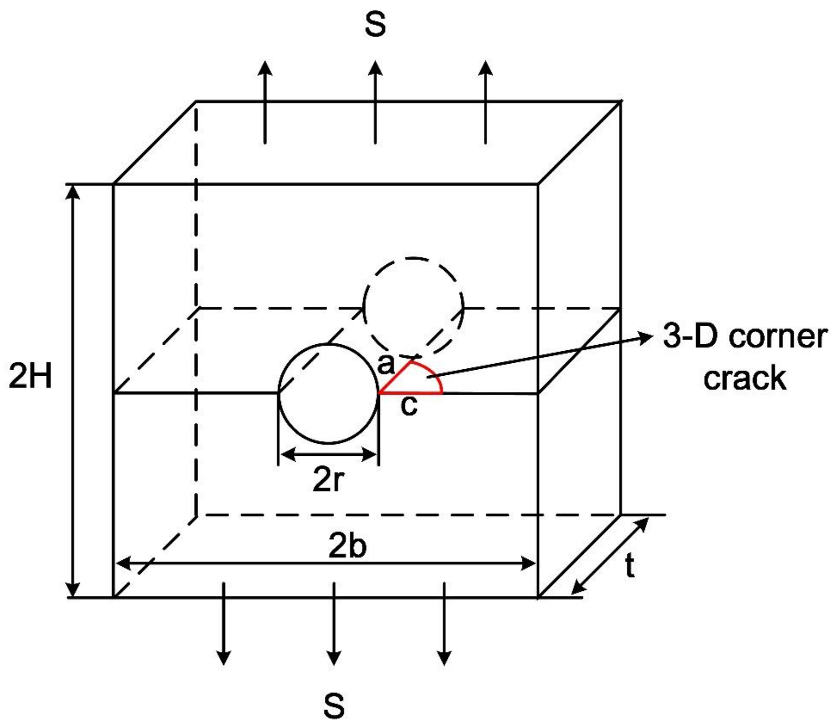

Figure 7. Schematic of a quarter-elliptical corner crack at a fastener hole.

Taking the plasticity-induced fatigue crack closure into account [63], which originates from the stress singularity at the crack tip, the SIF range, ΔK, used for calculating crack growth in Eq. (8), is replaced by the effective SIF range, ΔK_{eff}, which is defined as the difference in two SIFs respectively calculated under the maximum stress of the fatigue load and the crack opening stress. ΔK_{eff} has proven effectiveness in describing crack growth when the crack is embryonic. For fatigue crack growth subject to a constant fatigue load, the crack opening stress can be determined based on a strip yield model [64], as

$$\frac{S_{open}}{S_{max}} = \begin{cases} A_0 + A_1 R & R < 0 \\ A_0 + A_1 R + A_2 R^2 + A_3 R^3, & R \geq 0 \end{cases} \tag{10}$$

where

$$A_0 = (0.825 - 0.34\alpha + 0.05\alpha^2)[\cos(\pi S_{max} / 2\sigma_0)]^{1/\alpha}$$
$$A_1 = (0.415 - 0.071\alpha) S_{max} / \sigma_0$$
$$A_2 = 1 - A_0 - A_1 - A_3$$
$$A_3 = 2A_0 + A_1 - 1.$$

In the above, S_{open} and S_{max} are the crack opening stress and the maximum stress of the fatigue load, respectively. R is the stress ratio of the fatigue load; σ_0 is the flow stress of the waveguide which is taken as the average of the yielding stress and ultimate tensile strength of the material, and α is the stress constraint factor at the crack tip.

In the model, the crack front is discretized into a series of points, as shown schematically in **Fig. 8**, and respective increment of these discrete points as crack progresses, upon considering the effect of plastic-induced crack closure phenomenon, can be determined using Eq. (8) upon replacing ΔK with ΔK_{eff}, as follows

$$\Delta K_{eff} = K_{max} - K_{open} = \Delta K\left(\frac{1 - S_{open} / S_{max}}{1 - R}\right). \tag{11}$$

Based on the calculated crack growth increment of each discrete point on the crack front, and the propagation direction as specified in the second hypothesis in the above, the new position of each discrete point upon a single fatigue cycle can be predicted using the model. With a least square method, the newly formed crack front after a fatigue cycle can be fitted, and the length and depth of the crack can be ascertained accordingly.

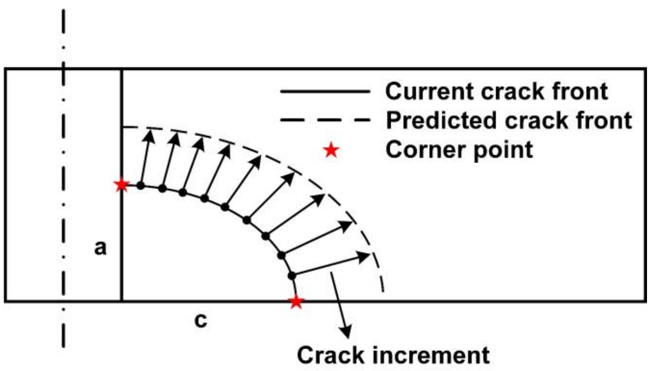

Figure 8. Crack front prediction as crack progresses using the proposed model (the current crack front is discretized into a series of points and crack increment of each point is calculated based on the Paris-Erdogan equation; the least square method is adopted to fit the newly formed crack front).

2.2.2 Model Validation

To verify the model, the growth and shape evolution of a series of quarter-elliptical corner cracks initiated from a fastener hole are predicted, and the predicted results are compared with those reported elsewhere [65]. The considered waveguide features a width ($2b$) of 80 mm, a height ($2H$) of 500 mm and a thickness (t) of 5 mm. Six quarter-elliptical corner cracks, each of which has a different initial aspect ratio (a/c), respectively emanating from the fastener hole of different radii (r/t = 0.5, 1.0 and 3.0, see **Fig. 7**) are considered. Initial depth, length and aspect ratio of the six corner cracks, respectively denoted by a_0, c_0 and $(a/c)_0$, are summarized in **Tab. 2**. Note that the two particular corner points on the crack front, as asterisked in **Fig. 8**, should be excluded during SIF calculation, as Eq. (9) is not applicable to these two points.

Table 2. Initial crack parameters in validation.

$(a/c)_0$	1.0	1.2	1.4	1.6	1.8	2.0
a_0 (mm)	1.0	1.0	1.0	1.0	1.0	1.0
c_0 (mm)	1.0	0.8333	0.7143	0.624	0.5556	0.5

As representative results, **Fig. 9** shows the correlation between the crack length and depth, as well as the shape evolution of three corner cracks when their initial aspect ratios are 1.0, 1.4 and 2.0, respectively, obtained using the predictive model in the offline phase. The predicted changes in the crack aspect ratio are compared with those obtained elsewhere [65], in **Fig. 10**, to observe quantitative accordance. In [40], the shape evolution of the same corner cracks under the same loading conditions is simulated using an FE approach.

In conclusion, the predicted results using the predictive model for the progress of a non-penetrating crack, at different initial aspect ratios and from a fastener hole of various radii, quantitatively tally with the earlier results, demonstrating the validity of the proposed 3-D crack growth model in predicting the growth and shape evolution of 3-D, non-penetrating fatigue cracks. With the predicted crack shape evolution, a quantitative correlation between the length and depth of a non-penetrating crack can further be established in the offline phase.

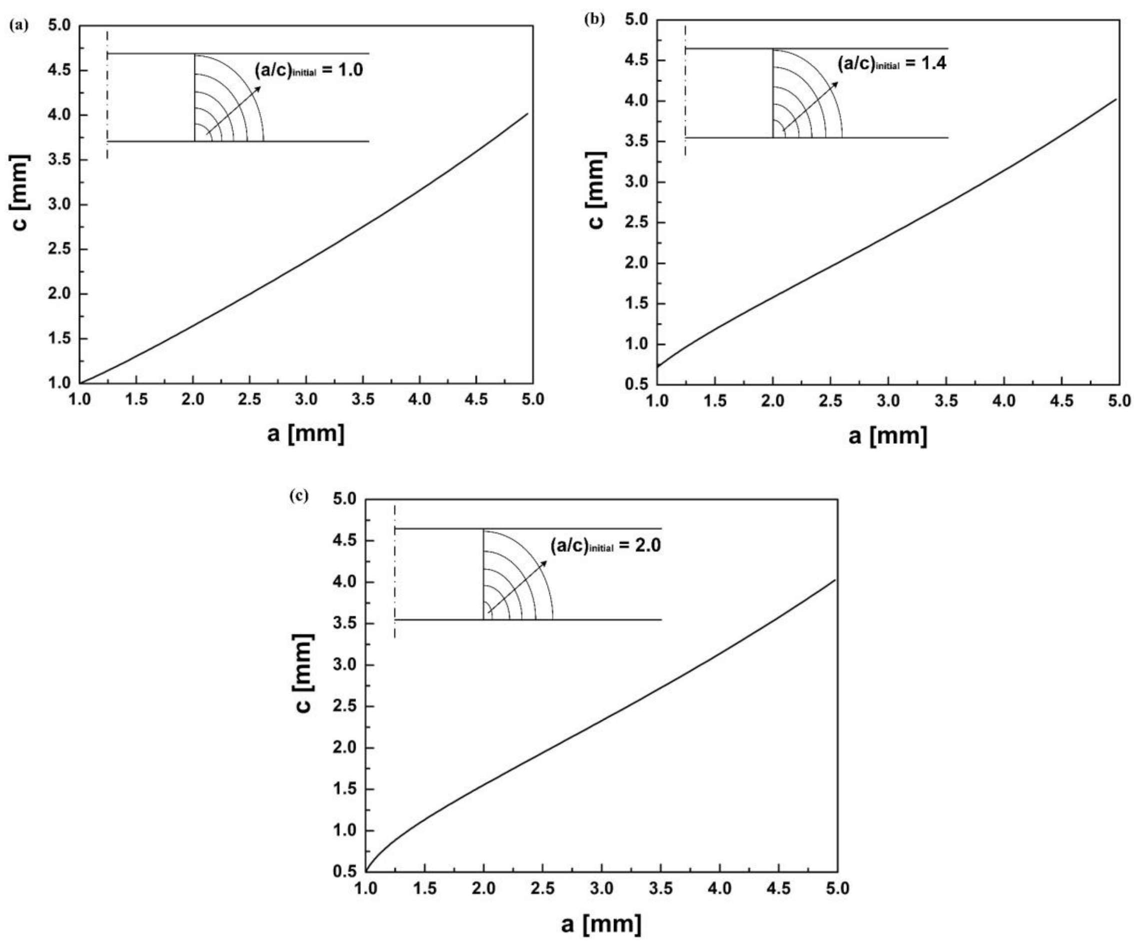

Figure 9. Predicted correlation between crack length and depth, and shape evolution (insert) of quarter-elliptical corner cracks using the predictive model in the offline phase, when (a) $(a/c)_0 = 1.0$; (b) $(a/c)_0 = 1.4$; and (c) $(a/c)_0 = 2.0$.

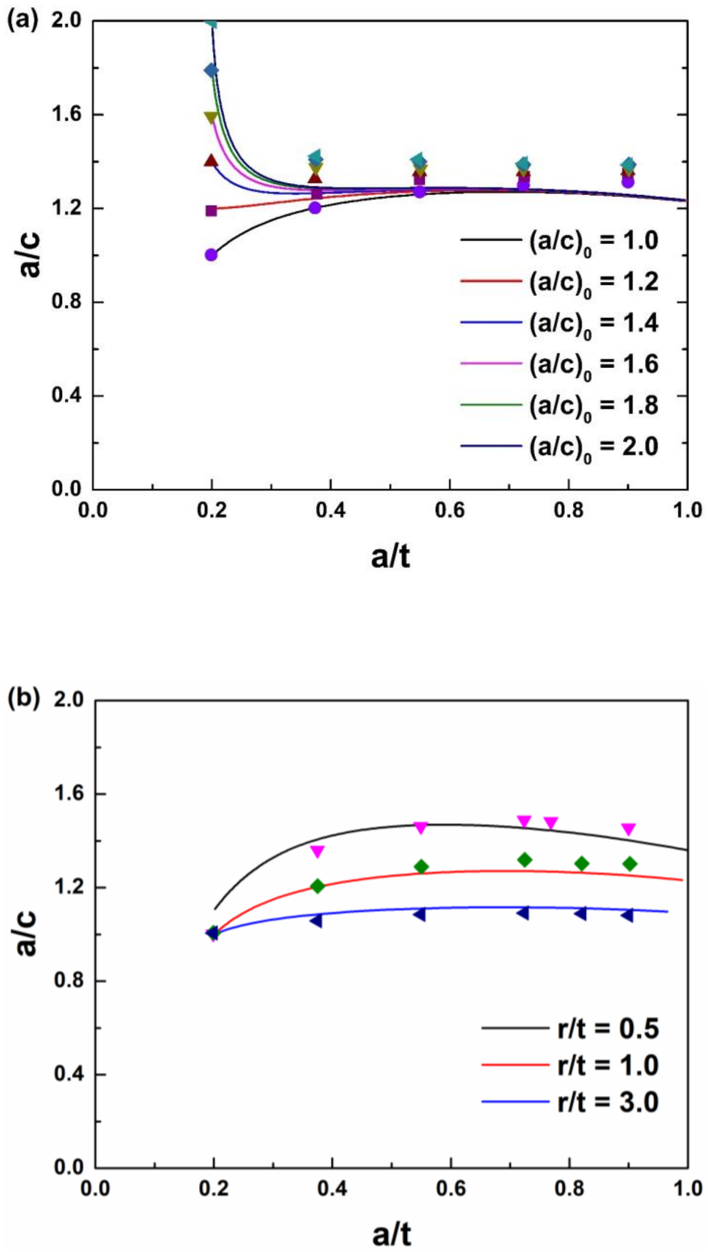

Figure 10. Predicted changes in aspect ratio of quarter-elliptical corner cracks, when (a) the crack is of different initial aspect ratios; and (b) the fastener hole is of different radii (curves: prediction based on the Newman-Raju equation [62]; dots: prediction by [40]).

2.3 Integrity of Online and Offline Phases

In the online phase, an analytical model based on the theory of elastodynamics sheds light on the generation of CAN in the probing GUWs under the modulation of the ‘breathing’ behavior of a non-penetrating fatigue crack, on which basis a crack-area-dependent damage index is created. Subsequent to the online phase, the fatigue crack growth model in the offline phase predicts further growth of the identified fatigue crack in its length and depth, based on the updated crack size obtained from the online phase, and establishes the relationship between the crack length and depth for later prediction. With both the online and offline phases, continuous and quantitative evaluation of non-penetrating fatigue crack is implemented. The schematic flowchart of the integrated two-step modeling framework is shown in **Fig. 11**.

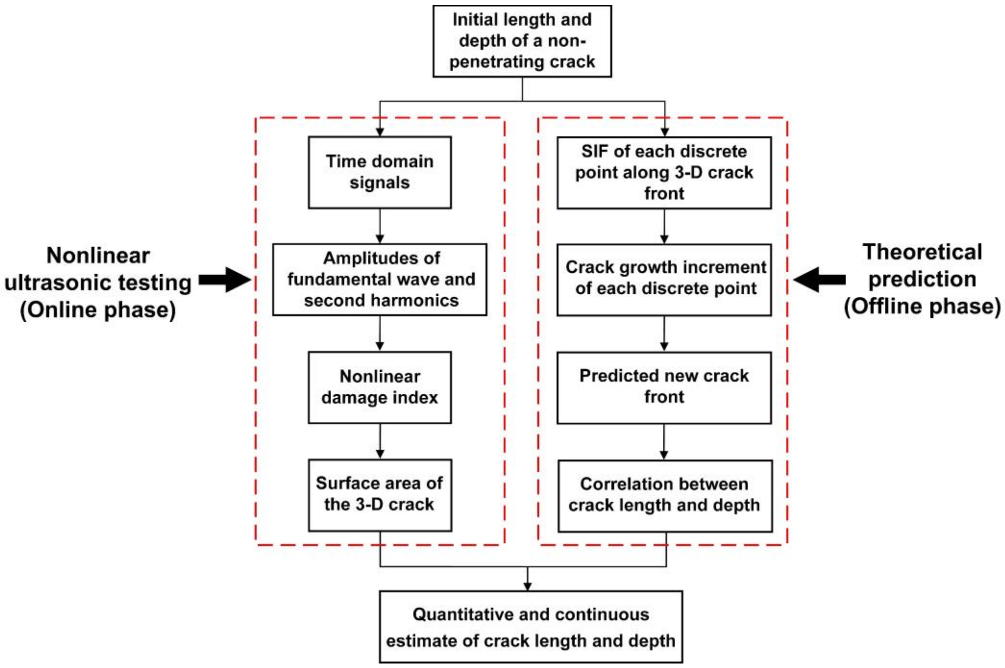

Figure 11. Flowchart of the developed two-step modeling framework for continuous monitoring and estimate of 3-D fatigue cracks, from initiation through growth (left column showing the online phase to identify crack surface area using nonlinear ultrasonic testing; right column showing the offline phase to predict change in aspect ratio and shape evolution of crack with 3-D crack growth model.

With the crack surface area that is estimated in the online phase and the correlation between the length and depth of the crack in the offline phase, the progress of a fatigue crack, from embryonic initiation, through progressive growth to the formation of macroscopic crack, can be evaluated quantitatively. It is noteworthy that no external loadings are included in modeling. For this sake, in practical implementation, the framework shall ideally be used in such a context.

3. Proof-of-Concept Experiment

Experiment is performed to validate the developed two-step modeling framework, by quantitatively evaluating a non-penetrating fatigue crack and continuously predict its growth under a fatigue load, until its formation into a macroscopic through-thickness crack. The experiment contains two hierarchical steps: 1) fatigue testing that drives the initial corner crack to progress under the fatigue load; and 2) nonlinear GUW-based testing that achieves continuous monitoring of the crack. **Figure 12** presents the pictured specimen and the schematic illustration of the nonlinear ultrasonic testing.

3.1 Fatigue Crack Growth Testing

An aluminium plate-like specimen (Aluminium 7075-T6; 500 mm long, 80 mm wide and 3 mm thick) is pre-treated with a through-thickness fastener hole (diameter: 6 mm) at the center of the specimen. To initiate a non-penetrating fatigue crack from the fastener hole edge, a tiny triangular notch, approximately 0.65 mm in its length and depth, respectively, is inscribed on the fastener hole edge in the plane perpendicular to the fatigue load direction.

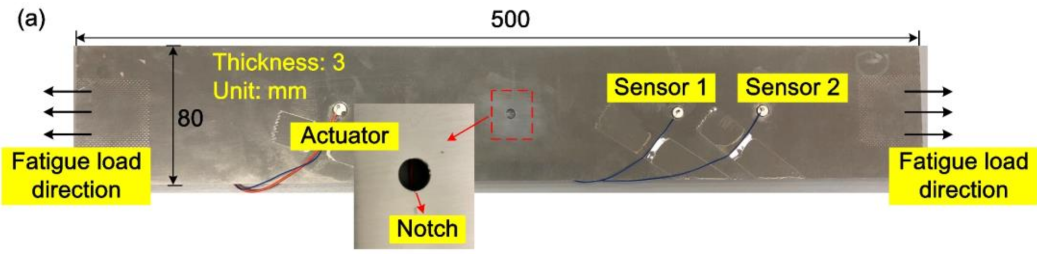

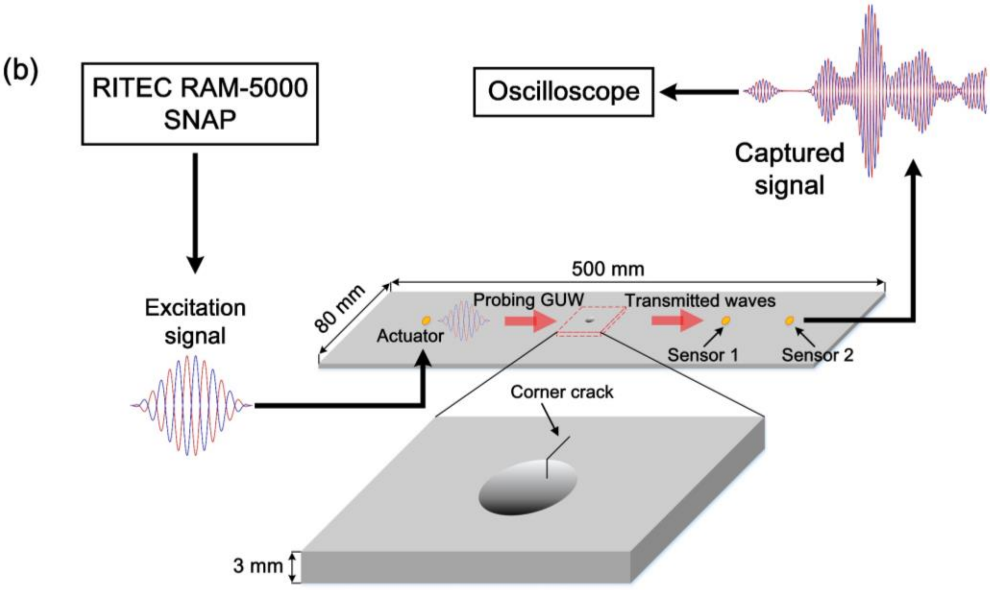

Figure 12. (a) Pictured specimen used in the fatigue testing (a PZT wafer functioning as GUW actuator and another two PZT wafers as sensors to capture wave signals); and (b) schematic of the nonlinear ultrasonic testing.

The crack growth testing is conducted on a fatigue testing platform (GP SDF2000). A 10 Hz pre-cracking cyclic load with the maximum tensile load of 30 kN and the stress ratio of 0.1 is applied, under which a corner crack is initiated from the tip of the inscribed notch on the fastener hold edge. The length and depth of the corner crack are real-time measured with a microscope and a flexible mirror inserted into the fastener hole, see **Fig. 13**. After the pre-cracking process, a quarter-elliptical corner crack is generated at the notch tip with ~1.0 mm in its length and depth, respectively. Subsequently, the cyclic load is regulated to 2~20 kN with a frequency of 10 Hz, to perform fatigue crack growth testing. The test is paused every 1,000 cycles; the length and depth of the corner crack are measured, and the nonlinear ultrasonic testing is performed during every pause. The test is terminated at 10,000 cycles, when the fatigue crack is observed to penetrate the specimen thickness. Typical photographs of the corner crack upon 0, 4,000, 8,000 and 10,000 load cycles are displayed in **Fig. 13**.

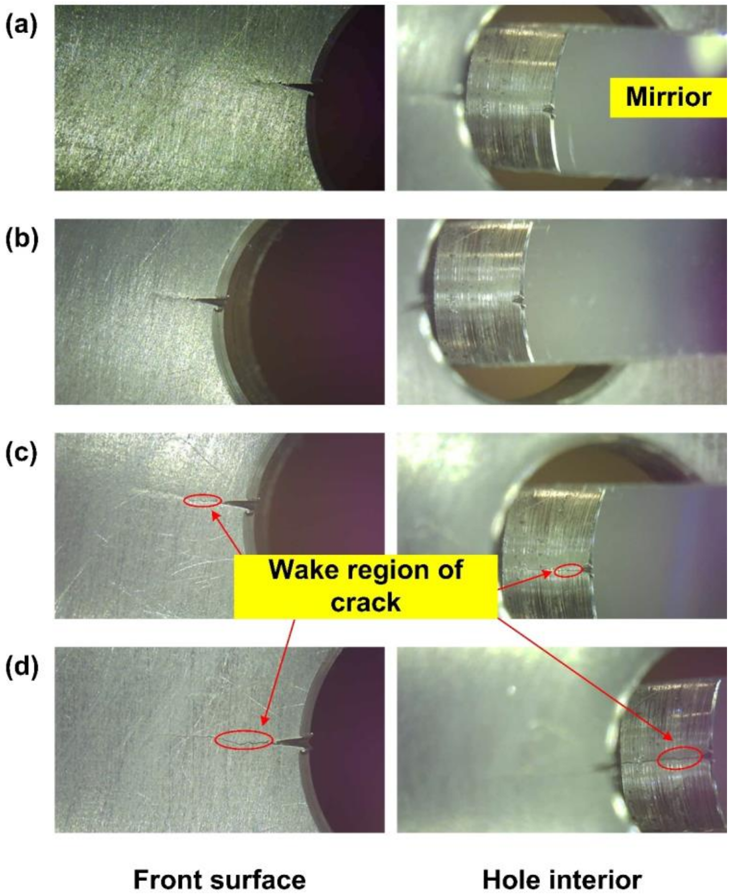

Figure 13. Photographs of the fatigue crack observed from the front surface of the specimen and from inside the fastener hole, upon (a) 0; (b) 4,000; (c) 8,000; and (d) 10,000 load cycles (after pre-cracking process, initial fatigue crack is generated; progress of the non-penetrating crack along the length and depth is observed at 4,000 and 8,000 load cycles, and a through-thickness crack is formed at 10,000 load cycles).

3.2 Quantitative Identification of Progressive Fatigue Crack (Online Phase)

During the pause of the fatigue crack growth testing (every 1,000 cycles), the nonlinear ultrasonic testing is carried out to capture and calibrate CAN induced by the 'breathing' crack. A lead zirconate titanate (PZT) wafer (PSN-33, diameter: 8 mm; thickness: 0.48 mm) is mounted on the surface of the specimen, 100 mm from the center of the fastener hole, which functions as a wave actuator to excite the probing GUW; two PZT wafers, same as the one used as the actuator, are mounted on the specimen 100 mm and 150 mm from the fastener hole, respectively, serving as the wave sensors, as shown in **Fig. 12**. All the three

PZT wafers are mounted on the specimen after the pre-cracking process, so that possible debonding between PZT wafers and the specimen can be avoided. A high-power ultrasonic testing system (RITEC®, RAM-5000 SNAP) is used to generate an Hanning-windowed 5-cycle sinusoidal toneburst at a central frequency of 250 kHz. Due to the small dimensions of the corner crack, the energy level of the incident GUWs is sufficient to modulate the crack and drive it to present 'breathing' behavior. The GUWs, upon interaction with the crack, are captured via two sensors with an oscilloscope at the sampling frequency of 200 MHz. Signals are averaged for 1,024 times to minimize the measurement uncertainty.

Figure 14 illustrates the GUW signals captured by two sensors upon 0, 4,000 and 8,000 load cycles. The variation in amplitudes of signals captured through the fatigue crack growth is within a small range of ~10%, implying a stable bonding condition between the PZT wafers and the specimen during the fatigue testing. This also argues that the change in signal amplitude – a linear feature of the GUW, is not sensitive to a fatigue crack in its embryonic stage. By using the pulse-inversion technique detailed in Section 2.1.2, the second order harmonics generated by the 'breathing' fatigue crack are obtained. **Figures 15(a)-(c)** show the signal spectra, captured by Sensor 2, as an example, upon 0, 4,000 and 8,000 load cycles applied, in which the crack-induced second order harmonics are observed. **Figure 15(d)** illustrates the amplitude of the second order harmonics at double excitation frequency (*i.e.*, 500 kHz), and it is apparent that the signal amplitude increases with respect to the number of load cycles.

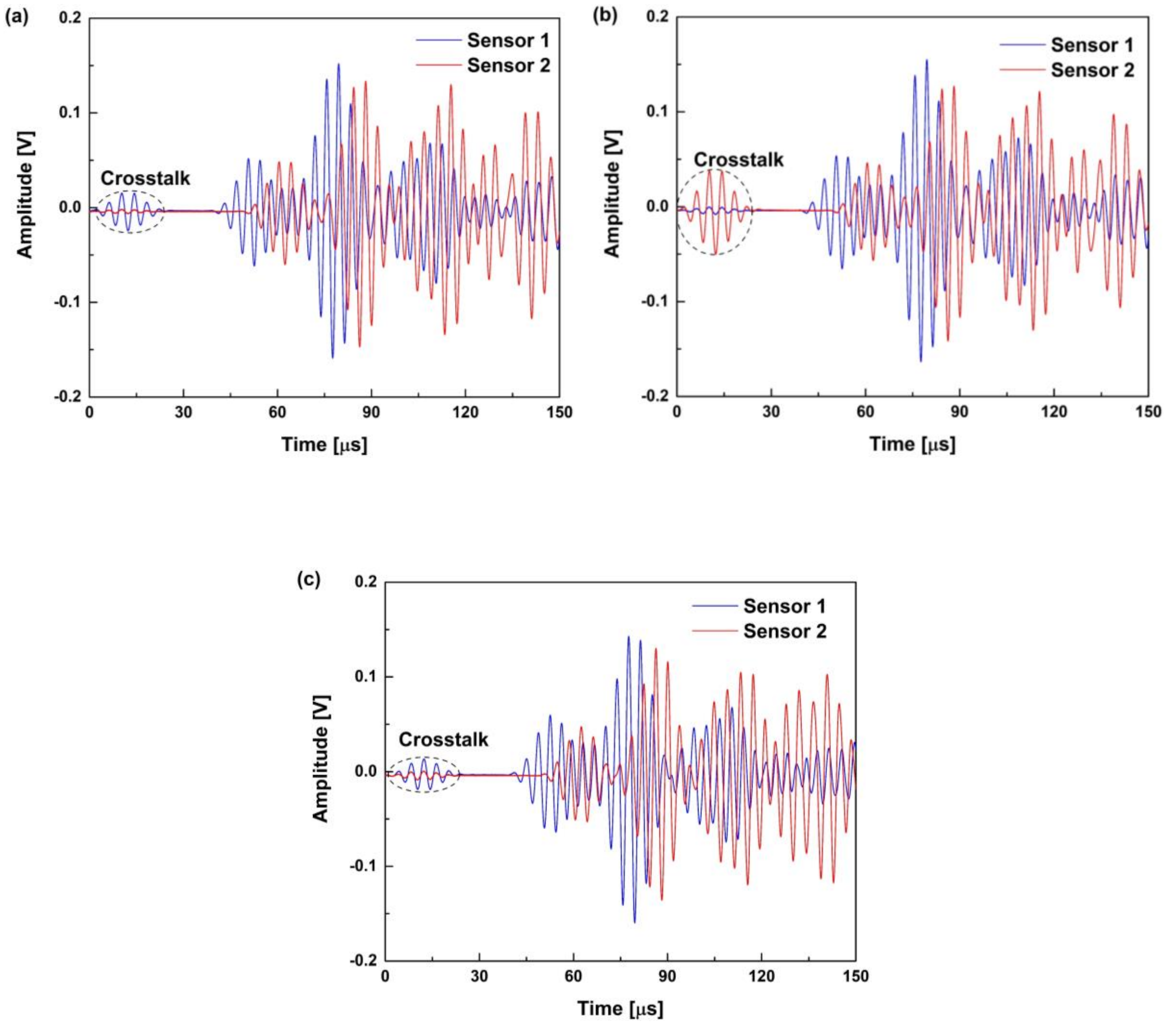

Figure 14. GUW signals captured by two sensors upon (a) 0; (b) 4,000; and (c) 8,000 load cycles (variation in amplitudes of signals captured through the fatigue crack growth is within a small range of ~10%, confirming a stable bonding condition between the PZT wafers and the specimen during the fatigue testing, and the change in signal amplitude (linear GUW feature) is not sensitive to incipient fatigue crack).

Based on the amplitudes of the captured GUW signals at fundamental frequency and of the second order harmonics at double excitation frequency, the nonlinear damage index is calculated using Eq. (7). Further, the relationship between the calculated index and the crack surface area (calculated with experimentally measured crack length and depth) is obtained, in **Fig. 16**.

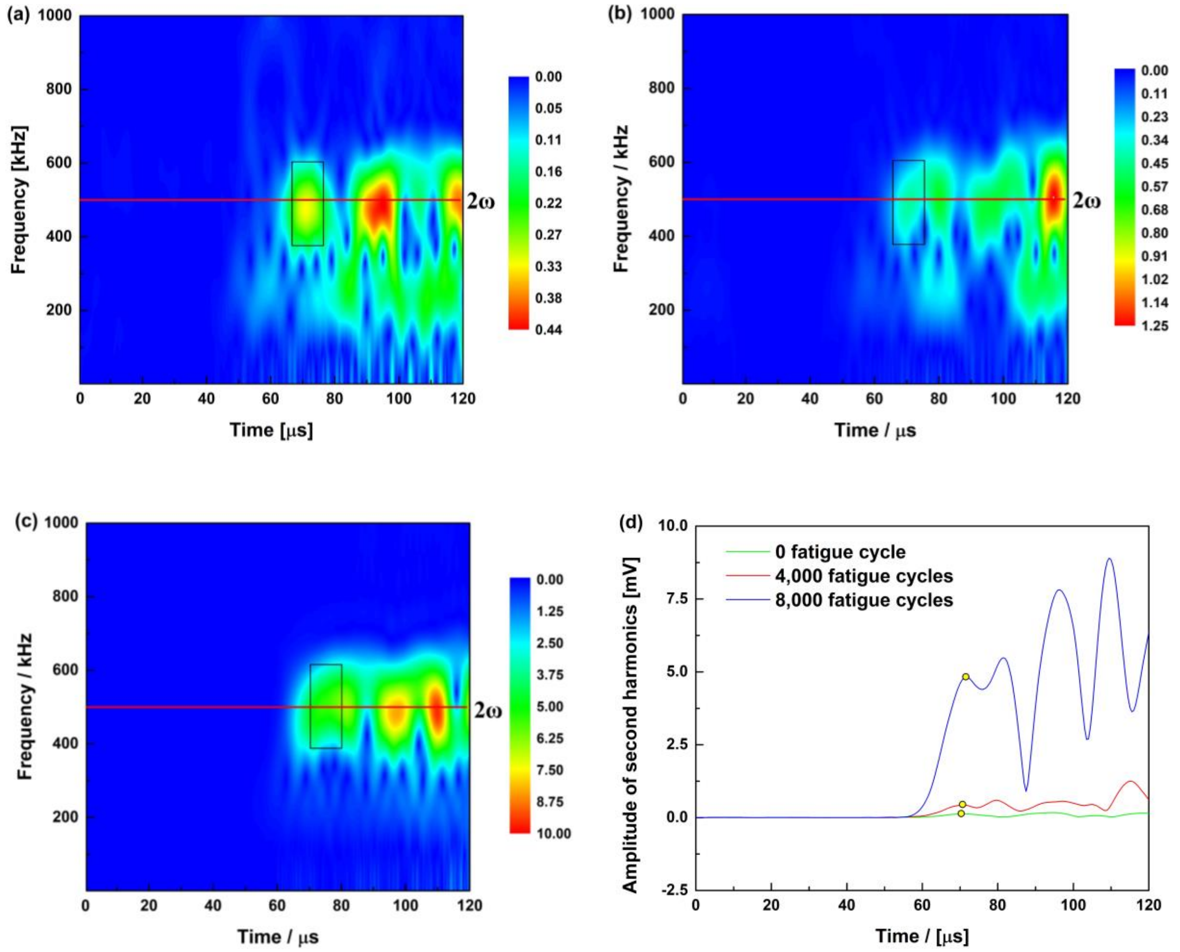

Figure 15. Spectra of signals captured by Sensor 2 (after applied with pulse-inversion technique), upon (a) 0; (b) 4,000; and (c) 8,000 load cycles; (d) amplitudes of the second order harmonics.

Note that in **Fig. 16**, the area of the crack surface generated in the pre-cracking stage (see Section 3.1) has been subtracted from the measured crack surface area, because it is not included in the correlation between the damage index and the severity of a fatigue crack in the modeling (Section 2). In **Fig. 16**, a proportional relationship between the calculated index and the measured crack surface area is observed, before the fatigue cycles reach 8,000, under which the crack surface area is smaller than 2 mm^2 and it represents an embryonic crack. The experimental results corroborate the conclusions that are drawn earlier from the analytical modeling and FE simulation in Section 2.1.2, not only verifying the proposed analytical modeling, also demonstrating the validity of the defined nonlinear damage index for evaluating the crack surface area.

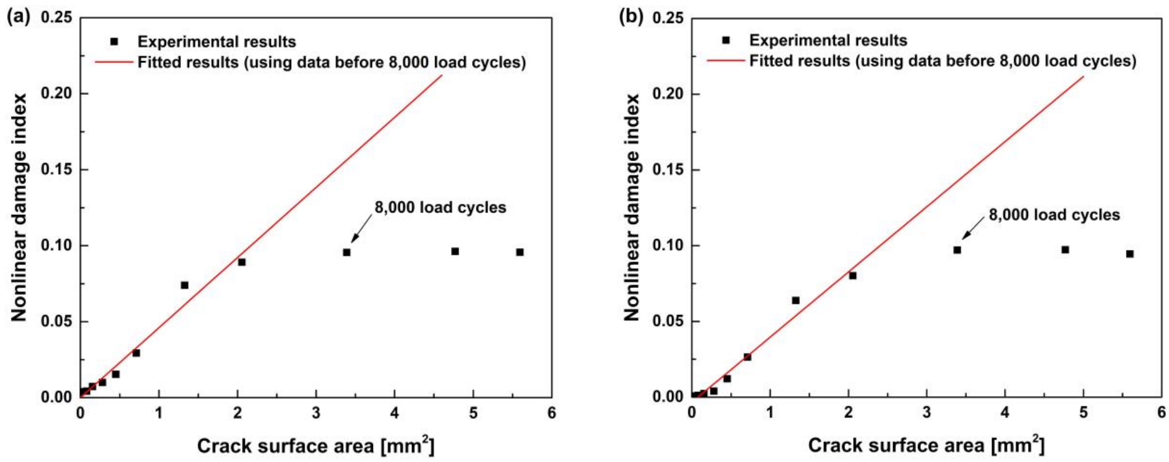

Figure 16. Nonlinear damage index calculated using signals captured by (a) Sensor 1; and (b) Sensor 2, versus experimentally measured crack surface area.

The indices obtained at 8,000 load cycles afterwards are lower than the fitted results, which can be attributed to two reasons: 1) the corner crack has grown to a considerable size after 8,000 load cycles and the crack opening displacement in the wake region of the crack is too large to present the 'breathing' behavior; 2) the compressive residual stress is generated at the crack tip as a result of the plastic deformation, which partly restrains the 'breathing' behavior of the fatigue crack.

3.3 Continuous Estimate of Progressive Fatigue Crack (Offline Phase)

To continuously estimate the crack growth along crack front, the offline phase is recalled to predict the change in aspect ratio of the corner crack as well as the crack shape evolution. Predicted results are presented in **Fig. 17**, compared with counterpart results experimentally measured, to observe good agreement.

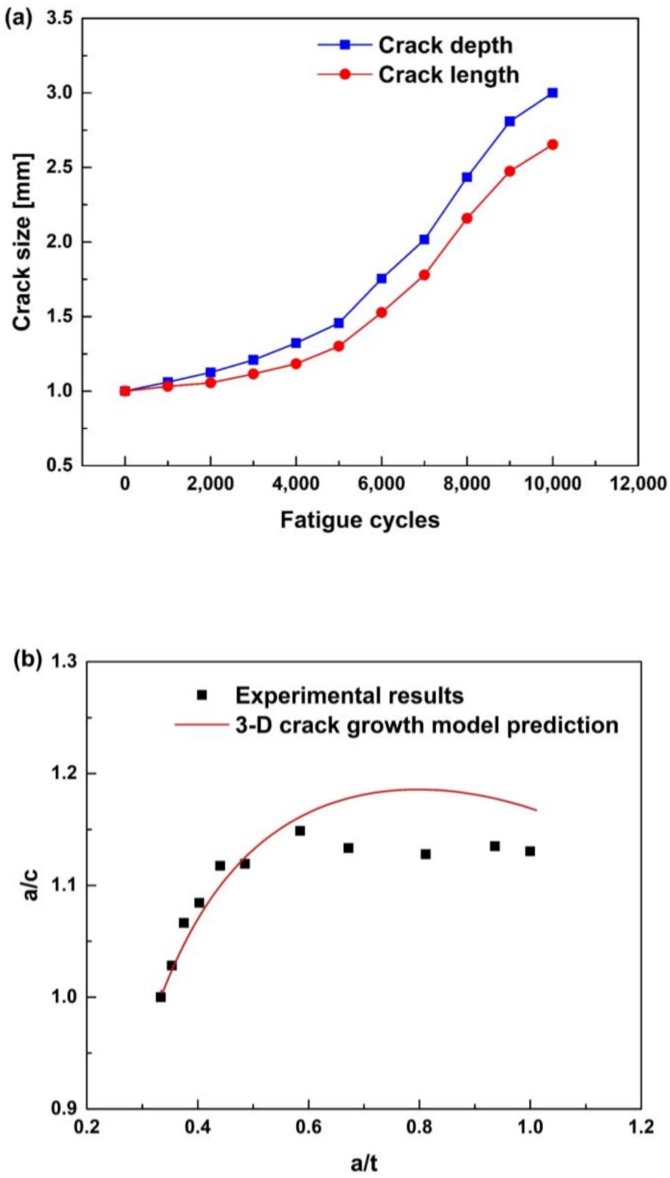

Figure 17. (a) Experimentally measured crack length and depth during its growth; (b) comparison between measured and predicted aspect ratios.

Combining the online and offline phases, **Fig. 18** shows the predicted length and depth of the corner crack, compared with experimentally measured results. The coincidence between predicted results and the reality has demonstrated that the two-step modeling framework is capable of identifying fatigue cracks at their embryonic stages (<8,000 fatigue load cycles), and predicting their growth along crack fronts, quantitatively and continuously.

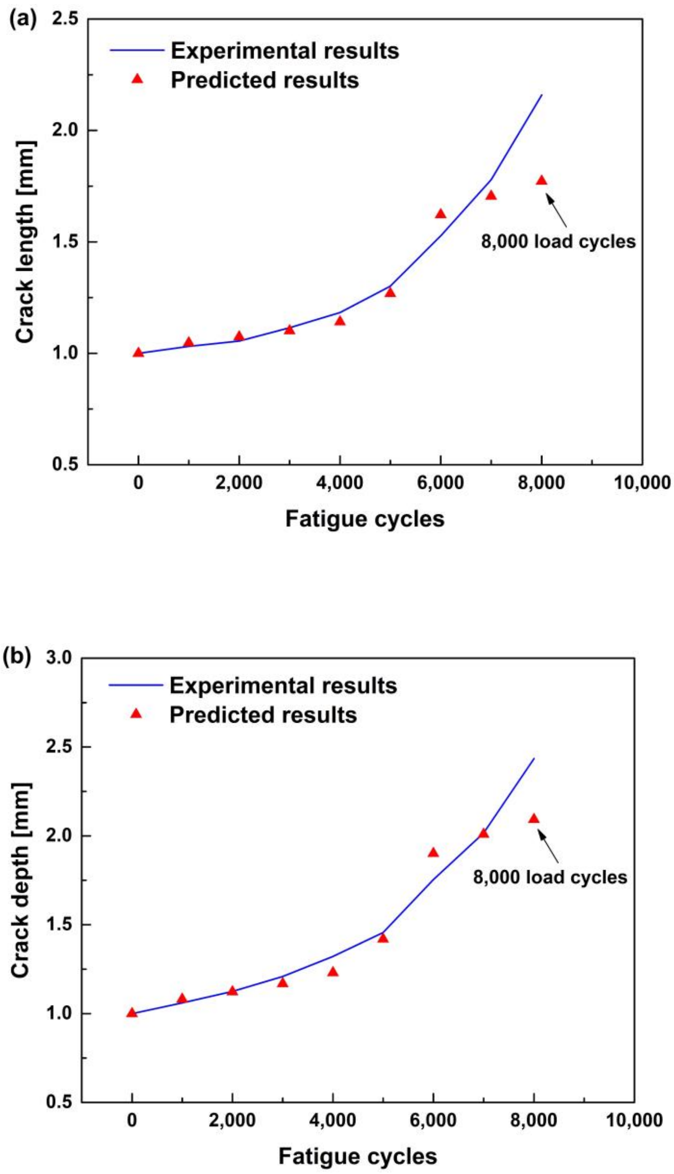

Figure 18. Experimentally measured (a) length and (b) depth of the corner crack during its growth, compared with predicted results using the modeling framework.

4. Concluding Remarks

It is of great significance yet a challenge to estimate fatigue cracks in engineering structures in their early stages. In this study, a two-step modeling framework, consisting of an online phase and an offline phase, is developed, which aims at continuously monitoring and quantitatively evaluating non-penetrating fatigue cracks. In the online phase, the 'breathing' crack-induced CAN is investigated analytically, by considering the nonlinear modulation of a fatigue crack on a probing GUW. A nonlinear damage index is defined and proven proportional to the crack surface area, highlighting the capability of the index for characterizing crack surface quantitatively. To predict growth of the identified fatigue crack in its length and depth along the crack front, a 3-D fatigue crack growth model is proposed in the offline phase. By investigating the crack growth increments of discrete points at the crack front, the growth of the crack along its crack front can be predicted, and the relationship between the length and depth of the crack is established. Proof-of-concept experiment is performed to validate the modeling framework. Good coincidence between the model-predicted and experimental results confirms the validity of the proposed two-step modeling framework for continuous monitoring and quantitatively evaluating fatigue cracks, from their embryonic initiation, through progressive growth to formation of macroscopic cracks.

Acknowledgments

The work was supported by a General Project (No. 51875492) and a Key Project (No. 51635008) received from the National Natural Science Foundation of China. Z Su acknowledges the support from the Hong Kong Research Grants Council via General Research Funds (Nos. 15202820, 15204419 and 15212417).

References

[1] K. Wang, Y. Li, Z. Su, R. Guan, Y. Lu, S. Yuan. Nonlinear aspects of “breathing” crack-disturbed plate waves: 3-D analytical modeling with experimental validation. Int. J. Mech. Sci. 2019;159:140-150.

[2] M. Chai, Z. Zhang, Q. Duan, Y. Song. Assessment of fatigue crack growth in 316LN stainless steel based on acoustic emission entropy. Int. J. Fatigue 2018;109:145-156.

[3] W. Jiang, Q. Zhang, Y. Zhang, Z. Guo, S.-T. Tu. Flexural behavior and damage evolution of pultruded fibre-reinforced composite by acoustic emission test and a new progressive damage model. Int. J. Mech. Sci. 2020;105955.

[4] S.F. Karimian, M. Modarres, H.A. Bruck. A new method for detecting fatigue crack initiation in aluminum alloy using acoustic emission waveform information entropy. Eng. Fract. Mech. 2020;223;106771.

[5] H. Cho, C.J. Lissenden. Structural health monitoring of fatigue crack growth in plate structures with ultrasonic guided waves. Struct. Health Monit. 2012;11(4):393-404.

[6] J. Li, Z.S. Khodaei, M. Aliabadi. Modelling of the high-frequency fundamental symmetric Lamb wave using a new boundary element formulation. Int. J. Mech. Sci. 2019;155:235-247.

[7] X. Ding, Y. Zhao, M. Deng, G. Shui, N. Hu. One-way Lamb mixing method in thin plates with randomly distributed micro-cracks. Int. J. Mech. Sci. 2020;171;105371.

[8] H. Bai, A. Shah, N. Popplewell, S. Datta. Scattering of guided waves by circumferential cracks in composite cylinders. Int. J. Solids Struct. 2002;39(17):4583-4603.

[9] A. de Pannemaecker, J. Buffiere, S. Fouvry, O. Graton. In situ fretting fatigue crack propagation analysis using synchrotron X-ray radiography. Int. J. Fatigue 2017;97:56-69.

[10] M. Connolly, M. Martin, P. Bradley, D. Lauria, A. Slifka, R. Amaro, C. Looney, J.-S. Park. In situ high energy X-ray diffraction measurement of strain and dislocation density ahead of crack tips grown in hydrogen. Acta Mater. 2019;180:272-286.

[11] A. Reid, M. Marshall, S. Kabra, T. Minniti, W. Kockelmann, T. Connolley, A. James, T. Marrow, M. Mostafavi. Application of neutron imaging to detect and quantify fatigue cracking. Int. J. Mech. Sci. 2019;159:182-194.

[12] G.P.M. Fierro, D. Ginzburg, F. Ciampa, M. Meo. Nonlinear ultrasonic stimulated thermography for damage assessment in isotropic fatigued structures. J. Sound Vib. 2017;404:102-115.

[13] S. Chhith, W. De Waele, P. De Baets, T. Van Hecke. On-line detection of fretting fatigue crack initiation by lock-in thermography. Tribol. Int. 2017;108:150-155.

[14] J. Qiu, C. Pei, H. Liu, Z. Chen, K. Demachi. Remote inspection of surface cracks in metallic structures with fiber-guided laser array spots thermography. NDT E Int. 2017;92:213-220.

[15] Y. Gao, G.Y. Tian, P. Wang, H. Wang, B. Gao, W.L. Woo, K. Li. Electromagnetic pulsed thermography for natural cracks inspection. Sci. Rep. 2017;7(1):1-9.

[16] I. Komura, T. Hirasawa, S. Nagai, J.-i. Takabayashi, K. Naruse. Crack detection and sizing technique by ultrasonic and electromagnetic methods. Nucl. Eng. Des. 2001;206(2-3):351-362.

[17] Z. Tong, S. Xie, H. Liu, W. Zhang, C. Pei, Y. Li, Z. Chen, T. Uchimoto, T. Takagi. An efficient electromagnetic and thermal modelling of eddy current pulsed thermography for quantitative evaluation of blade fatigue cracks in heavy-duty gas turbines. Mech. Syst. Sig. Process. 2020;142;106781.

[18] R. Xie, D. Chen, M. Pan, W. Tian, X. Wu, W. Zhou, Y. Tang. Fatigue Crack Length Sizing Using a Novel Flexible Eddy Current Sensor Array. Sensors (Basel) 2015;15(12):32138-32151.

[19] A. Rakow, F.-K. Chang. A structural health monitoring fastener for tracking fatigue crack growth in bolted metallic joints. Struct. Health Monit. 2011;11(3):253-267.

[20] C.G. Camerini, L.B. Campos, V.M. Silva, D.S. Castro, R.W. Santos, J.M. Rebello, G.R. Pereira. Correlation of eddy current signals obtained from EDM notches and fatigue cracks. J. Mater. Res. Technol. 2019;8(5):4843-4848.

[21] P. Kudela, W. Ostachowicz, A. Żak. Damage detection in composite plates with embedded PZT transducers. Mech. Syst. Sig. Process. 2008;22(6):1327-1335.

[22] T. Wandowski, P. Malinowski, W. Ostachowicz. Damage detection with concentrated configurations of piezoelectric transducers. Smart Mater. Struct. 2011;20(2):025002.

[23] X. Zhao, H. Gao, G. Zhang, B. Ayhan, F. Yan, C. Kwan, J.L. Rose. Active health monitoring of an aircraft wing with embedded piezoelectric sensor/actuator network: I. Defect detection, localization and growth monitoring. Smart Mater. Struct. 2007;16(4):1208.

[24] J. He, X. Guan, T. Peng, Y. Liu, A. Saxena, J. Celaya, K. Goebel. A multi-feature integration method for fatigue crack detection and crack length estimation in riveted lap joints using Lamb waves. Smart Mater. Struct. 2013;22(10):105007.

[25] F. Li, X. Sun, J. Qiu, L. Zhou, H. Li, G. Meng. Guided wave propagation in high-speed train axle and damage detection based on wave mode conversion. Struct. Control and Health Monit. 2015;22(9):1133-1147.

[26] Y. Shen, C.E. Cesnik. Nonlinear scattering and mode conversion of Lamb waves at breathing cracks: An efficient numerical approach. Ultrasonics 2019;94:202-217.

[27] Y. Shen, M. Cen, W. Xu, Scanning laser vibrometry imaging of fatigue cracks via nonlinear ultrasonic guided wave scattering and mode conversion, in: Health Monitoring of Structural and Biological Systems XIII, International Society for Optics and Photonics, 2019, pp. 109721I.

[28] Y. Koh, W.K. Chiu, N. Rajic. Effects of local stiffness changes and delamination on Lamb wave transmission using surface-mounted piezoelectric transducers. Compos. Struct. 2002;57(1-4):437-443.

[29] Y. Lu, L. Ye, Z. Su, C. Yang. Quantitative assessment of through-thickness crack size based on Lamb wave scattering in aluminium plates. NDT E Int. 2008;41(1):59-68.

[30] M. Matsushita, N. Mori, S. Biwa. Transmission of Lamb waves across a partially closed crack: Numerical analysis and experiment. Ultrasonics 2019;92:57-67.

[31] L. Zhu, Z.R. Wu, X.T. Hu, Y.D. Song. Investigation of small fatigue crack initiation and growth behaviour of nickel base superalloy GH4169. Fatigue Fract. Eng. Mater. Struct. 2016;39(9):1150-1160.

[32] N.B. McFadyen, R. Bell, O. Vosikovsky. Fatigue crack growth of semi-elliptical surface cracks. Int. J. Fatigue 1990;12(1):43-50.

[33] M. Ryles, F.H. Ngau, I. McDonald, W.J. Staszewski. Comparative study of nonlinear acoustic and Lamb wave techniques for fatigue crack detection in metallic structures. Fatigue Fract. Eng. Mater. Struct. 2008;31(8):674-683.

[34] K. Dziedziech, L. Pieczonka, P. Kijanka, W.J. Staszewski. Enhanced nonlinear crack-wave interactions for structural damage detection based on guided ultrasonic waves. Structural Control and Health Monitoring 2016;23(8):1108-1120.

[35] X. Guo, D. Zhang, J. Zhang. Detection of fatigue-induced micro-cracks in a pipe by using time-reversed nonlinear guided waves: a three-dimensional model study. Ultrasonics 2012;52(7):912-919.

[36] Z. Su, C. Zhou, M. Hong, L. Cheng, Q. Wang, X. Qing. Acousto-ultrasonics-based fatigue damage characterization: Linear versus nonlinear signal features. Mech. Syst. Sig. Process. 2014;45(1):225-239.

[37] Y. Yang, C.-T. Ng, A. Kotousov, H. Sohn, H.J. Lim. Second harmonic generation at fatigue cracks by low-frequency Lamb waves: Experimental and numerical studies. Mech. Syst. Sig. Process. 2018;99:760-773.

[38] G. Ren, J. Kim, K.-Y. Jhang. Relationship between second-and third-order acoustic nonlinear parameters in relative measurement. Ultrasonics 2015;56:539-544.

[39] J.-Y. Kim, V. Yakovlev, S. Rokhlin. Surface acoustic wave modulation on a partially closed fatigue crack. The Journal of the Acoustical Society of America 2004;115(5):1961-1972.

[40] I. Solodov, J. Wackerl, K. Pfleiderer, G. Busse. Nonlinear self-modulation and subharmonic acoustic spectroscopyfor damage detection and location. Appl. Phys. Lett. 2004;84(26):5386-5388.

[41] C.-S. Park, J.-W. Kim, S. Cho, D.-c. Seo. A high resolution approach for nonlinear sub-harmonic imaging. NDT E Int. 2016;79:114-122.

[42] D. Chronopoulos. Calculation of guided wave interaction with nonlinearities and generation of harmonics in composite structures through a wave finite element method. Compos. Struct. 2018;186:375-384.

[43] M. Sun, J. Qu. Analytical and Numerical Investigations of One-Way Mixing of Lamb Waves in a Thin Plate. Ultrasonics 2020;106180.

[44] K.-A. Van Den Abeele, P.A. Johnson, A. Sutin. Nonlinear elastic wave spectroscopy (NEWS) techniques to discern material damage, part I: nonlinear wave modulation spectroscopy (NWMS). Journal of Research in Nondestructive Evaluation 2000;12(1):17-30.

[45] A.M. Albishi, M.S. Boybay, O.M. Ramahi. Complementary Split-Ring Resonator for Crack Detection in Metallic Surfaces. IEEE Microwave Wireless Compon. Lett. 2012;22(6):330-332.

[46] H.J. Lim, H. Sohn. Online fatigue crack prognosis using nonlinear ultrasonic modulation. Structural Health Monitoring 2019;18(5-6):1889-1902.

[47] D.T. Zeitvogel, K.H. Matlack, J.-Y. Kim, L.J. Jacobs, P.M. Singh, J. Qu. Characterization of stress corrosion cracking in carbon steel using nonlinear Rayleigh surface waves. NDT E Int. 2014;62:144-152.

[48] G. Kim, C.-W. In, J.-Y. Kim, K.E. Kurtis, L.J. Jacobs. Air-coupled detection of nonlinear Rayleigh surface waves in concrete—Application to microcracking detection. NDT E Int. 2014;67:64-70.

[49] Y. Shen, V. Giurgiutiu, Predictive simulation of nonlinear ultrasonics, in: Health Monitoring of Structural and Biological Systems 2012, International Society for Optics and Photonics, 2012, pp. 83482E.

[50] Y.F. Lee, Y. Lu, R. Guan. Nonlinear guided waves for fatigue crack evaluation in steel joints with digital image correlation validation. Smart Mater. Struct. 2020;29(3):035031.

[51] R. Guan, Y. Lu, K. Wang, Z. Su. Fatigue crack detection in pipes with multiple mode nonlinear guided waves. Structural Health Monitoring 2019;18(1):180-192.

[52] K. Wang, M. Liu, Z. Su, S. Yuan, Z. Fan. Analytical insight into "breathing" crack-induced acoustic nonlinearity with an application to quantitative evaluation of contact cracks. Ultrasonics 2018;88:157-167.

[53] K. Wang, Z. Fan, Z. Su. Orienting fatigue cracks using contact acoustic nonlinearity in scattered plate waves. Smart Mater. Struct. 2018;27(9):09LT01.

[54] J. Shi, D. Chopp, J. Lua, N. Sukumar, T. Belytschko. Abaqus implementation of extended finite element method using a level set representation for three-dimensional fatigue crack growth and life predictions. Eng. Fract. Mech. 2010;77(14):2840-2863.

[55] B. Masserey, P. Fromme. In-situ monitoring of fatigue crack growth using high frequency guided waves. NDT E Int. 2015;71:1-7.

[56] B. Masserey, P. Fromme. Fatigue crack growth monitoring using high-frequency guided waves. Structural Health Monitoring 2013;12(5-6):484-493.

[57] B. Masserey, P. Fromme. Analysis of high frequency guided wave scattering at a fastener hole with a view to fatigue crack detection. Ultrasonics 2017;76:78-86.

[58] L. Śnieżek, T. Ślęzak, K. Grzelak, V. Hutsaylyuk. An experimental investigation of propagation the semi-elliptical surface cracks in an austenitic steel. Int. J. Press. Vessels Pip. 2016;144:35-44.

[59] J.D. Achenbach, Y. Xu. Wave motion in an isotropic elastic layer generated by a time-harmonic point load of arbitrary direction. The Journal of the Acoustical Society of America 1999;106(1):83-90.

[60] Y. Ohara, K. Kawashima, R. Yamada, H. Horio, Evaluation of amorphous diffusion bonding by nonlinear ultrasonic method, in: AIP Conference Proceedings, American Institute of Physics, 2004, pp. 944-951.

[61] A. Grandt Jr, D. Macha. Digitized measurements of the shape of corner cracks at fastener holes. Eng. Fract. Mech. 1983;17(1):63-73.

[62] J. Newman, I. Raju, Stress-intensity factor equations for cracks in three-dimensional finite bodies, in: Fracture Mechanics: Fourteenth Symposium—Volume I: Theory and Analysis, ASTM International, 1983.

[63] E. Wolf. Fatigue crack closure under cyclic tension. Eng. Fract. Mech. 1970;2(1):37-45.

[64] J. Kim, S.-B. Lee. Fatigue crack opening stress based on the strip-yield model. Theor. Appl. Fract. Mech. 2000;34(1):73-84.

[65] X. Lin, R. Smith. Fatigue shape analysis for corner cracks at fastener holes. Eng. Fract. Mech. 1998;59(1):73-87.